Single and Multiple Doping in Graphene Quantum Dots: Unraveling the Origin of Selectivity in the Oxygen Reduction Reaction

Marco Favaro,[†] Lara Ferrighi,[‡] Gianluca Fazio,[‡] Luciano Colazzo,[†] Cristiana Di Valentin,*,[‡] Christian Durante,[†] Francesco Sedona,[†] Armando Gennaro,[†] Stefano Agnoli,*,[†] and Gaetano Granozzi[†]

[†]Department of Chemical Sciences, Università degli studi di Padova, Via Marzolo 1, 35131 Padova, Italy
[‡]Dipartimento di Scienza dei Materiali, Università di Milano-Bicocca, Via Cozzi 53, 20125 Milano, Italy

Ⓢ *Supporting Information*

ABSTRACT: Singly and multiply doped graphene oxide quantum dots have been synthesized by a simple electrochemical method using water as solvent. The obtained materials have been characterized by photoemission spectroscopy and scanning tunneling microscopy, in order to get a detailed picture of their chemical and structural properties. The electrochemical activity toward the oxygen reduction reaction of the doped graphene oxide quantum dots has been investigated by cyclic voltammetry and rotating disk electrode measurements, showing a clear decrease of the overpotential as a function of the dopant according to the sequence: N ∼ B > B,N. Moreover, assisted by density functional calculations of the Gibbs free energy associated with every electron transfer, we demonstrate that the selectivity of the reaction is controlled by the oxidation states of the dopants: as-prepared graphene oxide quantum dots follow a two-electron reduction path that leads to the formation of hydrogen peroxide, whereas after the reduction with $NaBH_4$, the same materials favor a four-electron reduction of oxygen to water.

KEYWORDS: *graphene, graphene oxide quantum dots, doped-quantum dots, multidoping, electrochemical preparation, oxygen reduction reaction, density functional theory*
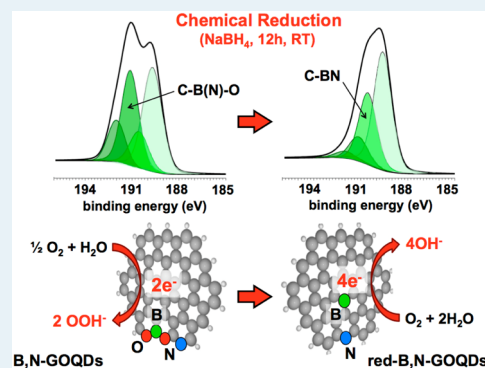
1. INTRODUCTION

Graphene (G) is the most fundamental archetype of carbon nanostructures, and it has gained a clear standing among materials due to its exceptional properties (superb carrier mobility, good transparency, excellent thermal conductivity, etc.). Nowadays, the forefront of research has moved from the study of the basic properties of pure G to the investigation of chemically modified G (CMG) systems,[1] i.e. doped or functionalized G, and of their composites with other nano-objects, such as nanoparticles and complex molecules. In contrast to the chemical inertness of G, CMGs present a remarkable reactivity, which stems either from defects or from new chemical functionalities. Among CMGs, G oxide (GO)[2] has gained a central role in G technology because it exhibits a tunable electric conductivity[3] and it can be easily obtained by the oxidation/exfoliation of graphite and processed to obtain wafer scaled devices.[4] Moreover, its solubility in water and facile functionalization make it a workhorse for wet chemistry applications.[3]

Together with GO, N-doped G is the other main player in the CMG arena. To prepare this material, several preparation methods were developed:[5] e.g., electrochemical reaction with NH_3,[6] exposure to nitrogen plasma,[7] chemical vapor deposition on metals (Cu and Ni) using a mixture of hydrocarbons, hydrogen, and nitrogen-containing molecules (NH_3,[8] pyridine,[9]

triazine[10]), pyrolysis of polymers,[11] solvothermal synthesis,[12] and the chemical reaction between GO and melamine.[13] N-doped G immediately aroused a great deal of attention because, differently from pure G, it shows promising activity as a metal-free electrocatalyst in the oxygen reduction reaction (ORR).[5,8,14]

Recently, other doped G sheets were prepared by different routes:[15,16]

(i) S-doped G by reaction of GO with benzyl disulfide[17] or by thermal exfoliation in sulfur-containing gases[18]

(ii) B-doped G by arc discharge of graphite electrodes in the presence of a H_2 and B_2H_6 mixture[19] or by annealing GO with B_2O_3[20] or even other methods[21,22]

(iii) F-doped G by CF_4 plasma treatment of pure G[23] or by arc discharge of graphite fluoride[24]

Lately, most advanced synthetic strategies have focused on the introduction of a combination of heteroatoms in G, leading to the preparation of B−N,[25−27] S−N,[28,29] and P−N[14] dually doped materials. These doped G systems exhibit quite interesting properties in terms of electroactivity, in particular

Table 1. Experimental Conditions for the Synthesis of Doped GOQDs

	electrolyte	dopant molecule[a]	final pH[b]	label
GOQDs	PBS 0.1 M (pH 6.86)		6.86	A
B-GOQDs	PBS 0.1 M (pH 11.20)[c]	1,4-phenylenebis(boronic acid) (**1**) (100 mM)	11.20	B
N-GOQDs	PBS 0.1 M (pH 6.86)	(a) ethylenediamine (**2**) (100 mM)	11.30	C
	PBS 0.1 M (pH 1.85)[d]	(b) 1,10-phenanthroline (**3**) (100 mM)	1.85	D
B,N-GOQDs	PBS 0.1 M (pH 6.86)	ethylenediamine (100 mM) + 1,4-phenylenebis(boronic acid) (100 mM)	11.30	E

[a]See Figure 1. The quantity of the dopant added was determined in order to obtain a final dopant volumetric concentration of 100 mM. [b]The pH was measured after the addition of the dopant molecule to the 0.1 M buffer solution. [c]The pH was increased by adding a few drops of a 10 M NaOH solution, in order to solubilize the doping molecules. [d]The pH was decreased by adding a few drops of concentrated H_3PO_4 (85%), in order to solubilize the 1,10-phenanthroline (by protonation of the pyridine nitrogens).

in the case of the ORR,[16,26,27] but also for alcohol oxidation and hydration reactions.[30,31]

Very recently, amidst CMGs, G quantum dots (GQDs) have emerged as a new class of materials with outstanding properties. They can be considered as small G patches, with a thickness of one or a few layers and with lateral dimensions below 10 nm. Differently from standard G materials, they are better described as macromolecules and are typically semiconductive with a clear separation between the HOMO and LUMO, which is strongly dependent on the geometrical size. Therefore, they also exhibit active optical properties such as photo- and electroluminescence and light upconversion, opening the door toward applications in photonics, optoelectronics, and photocatalysis.[32]

Moreover, due to their small dimension, GQDs can be easily interfaced to other nano-objects in order to build more complex systems. Similarly to other CMGs, GQDs can also be doped with heteroatoms or functionalized with specific chemical species. This high versatility in the design of complex systems and the easy tunability of their physical properties have generated an immediate interest in the scientific community. GQDs have quickly found application as nanolights for bioimaging[32,33] and sensitizers for photocatalytic systems,[34] and they are envisaged to support a full gamut of practical applications, ranging from road signs and fluorescent clothing to biological markers in medical research.[35]

In a recent paper we have demonstrated that, using a simple electrochemical (EC) procedure starting from GO electrodes, GOQD solutions can be easily prepared.[36] Here we report a further development of this method providing a systematic description of the preparation and characterization of singly (B and N) and multiply doped (N and B) GOQDs. We studied their chemical reactivity toward ORR, observing a clear improvement of the catalytic activity in the presence of the single dopants, which is further boosted when both B and N are present. Furthermore, DFT calculations were performed in order to rationalize and shed new light on the observed reactivity toward the reduction of oxygen. We found that the ORR selectivity in GOQDs can be switched quite easily from a $2e^-$ to a $4e^-$ path simply by chemically reducing the doped materials. The presence of oxygen functional groups therefore represents a pivotal factor for controlling the chemical selectivity, which so far has been completely overlooked. This work therefore provides a basic understanding for a rational design of ORR electrocatalysts operating at very small overpotential that can either selectively reduce oxygen to water or, when oxidized, efficiently produce hydrogen peroxide.

2. EXPERIMENTAL SECTION

Only basic information is reported in the present section. See the Supporting Information for more details.

The preparation of GO microflakes was performed using the modified Hummers oxidation reaction.[37,38] The characterization of the starting GO material was carried out by X-ray photoemission spectroscopy (XPS), Fourier transform infrared reflectance absorption spectroscopy (FT-IRAS), UV−vis absorption spectroscopy, and Raman microscopy (Figure S1, Supporting Information). The lateral dimensions of the GO sheets were determined by scanning electron microscopy (SEM) measurements with the GO sheets deposited by means of anodic electrophoretic deposition on P:Si (100) wafers.[36] The statistical analysis of GO microflake size is characterized by a wide distribution, which ranges from 1 to 5 μm. The SEM results obtained on the GO single layers and on the GO thin films are reported in Figure S2 (Supporting Information).

The EC preparation of GOQDs[36,39,40] was carried out at 25 °C in a standard three-electrode EC cell, using a Pt ring as the counter electrode (CE) and a saturated Ag/AgCl/Cl⁻ electrode as the reference electrode (RE), cycling the potential between ±3.000 V (−2.803 to +3.197 V vs SHE) at a scan rate of 500 mV/s (see Figure S3, Supporting Information).

The working electrodes (WEs) were built by depositing a GO thin film (Figure S1, Supporting Information) on a polished glassy-carbon (GC) substrate. The EC syntheses of doped GOQDs were carried out by adding to a 0.1 M phosphate buffer solution (PBS) the molecular precursor chosen as the dopant source.

The pure and doped GOQDs were then collected after about 2000 potential cycles. Table 1 reports the experimental conditions for the different syntheses.

More details on the procedures and methods are reported in the Supporting Information. Thin films of GOQDs drop-cast on polycrystalline copper foils were used for the SEM and XPS characterizations. Technical details are provided in the Supporting Information.

The electrochemical activity measurements toward the ORR were carried out by cyclic voltammetry (CV) and rotating disk electrode (RDE) voltammetry. A conventional three-electrode configuration consisting of a Pt wire as the CE and a saturated Ag/AgCl/Cl⁻(sat.) as the RE was used (standard electrode potential $E°_{Ag/AgCl(sat.)} = 0.197$ V with respect to the standard hydrogen electrode, SHE). All potentials reported in this work are referenced to the SHE.

In order to prepare the catalyst ink, 4 mg of the pure or doped GOQD was dissolved in 1 mL of doubly distilled water; after the addition of perfluorinated Nafion alcoholic solution (5%, Aldrich), the obtained solution was ultrasonicated for 30 min. Then, the WE was prepared by depositing 15 μL of the ink onto a polished GC disk mounted on a RDE tip (Autolab RDE-2), which exposed an area of 0.071 cm² to the electrolyte.
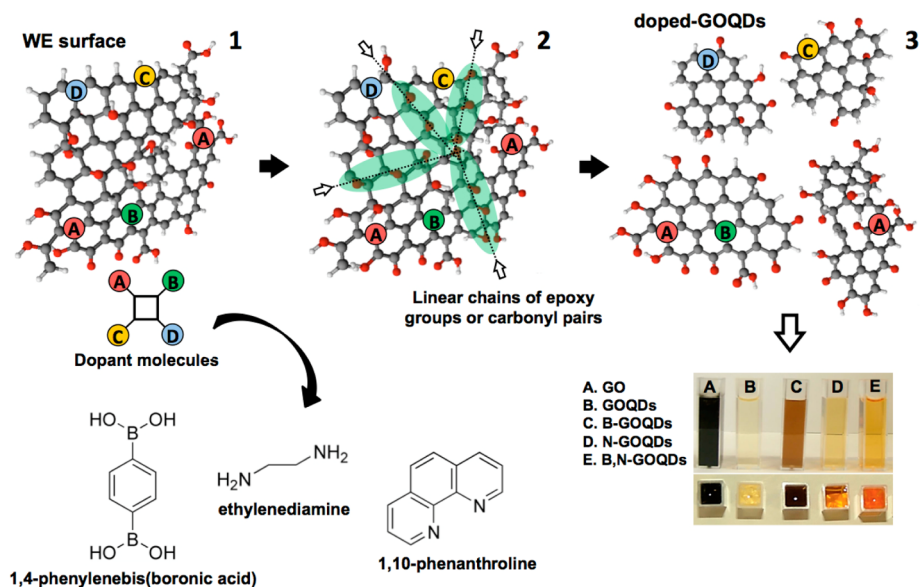
Figure 1. Pictorial model of the doping mechanism occurring during the synthesis of doped GOQDs, reporting the molecular structures of the dopant molecules used in this work (1,4-phenylenebis(boronic acid), ethylenediamine, and 1,10-phenanthroline).

Finally, the drop-casted film was dried in air at room temperature for about 12 h.

All calculations were performed with the GAUSSIAN09[41] (G09) package and the B3LYP[42,43] functional. Spin polarization was taken into account in the case of open-shell systems. The model for pure G QDs is a circumcoronene molecule ($C_{54}H_{18}$). The orbitals were described with the Gaussian basis function 6-311+G* for the inner five C atoms, the B and N atoms, and the O and H atoms involved in the water formation; the basis function 6-31G* was used for the rest of the model. All atoms were allowed to relax during the geometry optimization without any symmetry constraint.

Vibrational frequencies in the harmonic approximation were calculated for all optimized structures and used, unscaled, to compute zero-point energies, enthalpies, and Gibbs free energies.

The conventional theoretical reference electrode is the standard hydrogen electrode, SHE.[44] At pH 0 and at the potential $U = 0$ V vs SHE, the reaction $H^+ + e^- \leftrightarrow {}^1/_2 H_2$ is in equilibrium at 1 bar of $H_2(g)$ at 298 K; thus, $G(H^+ + e^-) = G({}^1/_2 H_2)$. The free energy difference of the full ORR with the present setup is −4.64 eV, which we consider to be in more than satisfactory agreement with the experimental value of −4.92 eV. The free energy of OH^- is derived as $G(OH^-) = G(H_2O(l)) - G(H^+)$, where $G(H^+)$ is corrected by $-kT \ln 10 \times pH$, to account for the pH conditions. However, for a direct comparison with experiments, the potential U values discussed later in the text (section 3.4) are referenced to the saturated Ag/AgCl/Cl⁻(sat.) reference electrode.

The contribution of bulk solvent (water) effects to the Gibbs free energy (G_{sol}) was computed using the polarizable continuum model (PCM) in the SMD version[45,46] implemented in the Gaussian09 package.

3. RESULTS AND DISCUSSION

3.1. Preparation. In this work, in order to avoid misinterpretation, we will use the following nomenclature: "graphene oxide quantum dots" (GOQDs) to indicate the as-prepared, oxidized materials, "reduced GOQDs" (red-GOQDs)
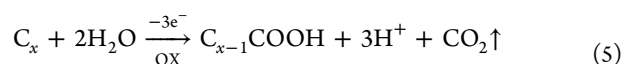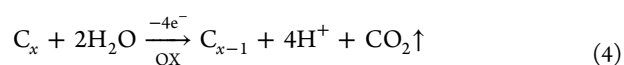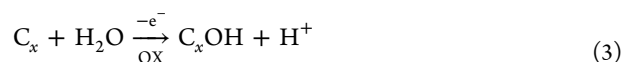
to refer to the chemically reduced materials, and "graphene QDs" (GQDs) as a general term that can indicate both types, reduced and oxidized, of quantum dots.

The electrochemical etching of an electrode constituted by G can produce a solution of highly luminescent GQDs.[39,53] A suitable change of the experimental conditions (i.e., solvent, supporting electrolyte, etc.) allows the preparation of doped Gs or GOQDs.[47,51] In particular, the use of an aqueous environment for the synthesis of GOQDs is more economical and environmentally friendly and poses fewer problems regarding the purification of the final product.[48] To the best of our knowledge, only the present study (along with the recent work on B-doped G quantum dots (GQDs) by Fan et al.[49]) reports the electrochemical synthesis of doped and codoped GOQDs by adding a molecular dopant precursor to an aqueous electrolytic medium. For the synthesis of doped GOQDs (as described in Table 1 and the Supporting Information), a dopant molecule (e.g., 1,4-phenylenebis(boronic acid), ethyl-enediamine, 1,10-phenanthroline) was added to the electrolyte solution to provide the doping heteroatoms. Similarly, to prepare codoped systems as B,N-GOQDs, a mixture of dopant molecules was introduced into the electrochemical cell.

The electrochemically assisted formation of GOQDs involves the oxidation of the C–C bonds and the intercalation of the electrolyte ions into the structure of the GO electrode, with the consequent release in solution of the GOQDs.[36,48,50]

Since the synthesis occurs under drastic conditions (i.e., corresponding to an applied potential when water is dissociated into molecular oxygen and hydrogen (eqs 1 and 2), a huge amount of highly reactive radicals is formed, either on the WE surface (eqs 3–5) or on the dopant molecules within the electrical double-layer region (Figure 1, step 1), as a result of their interactions with radicals from the dissociation of water:[49,50]

$$H_2O \xrightarrow[\text{OX}]{-2e^-} 2H^+ + {}^1/_2 O_2 \uparrow \qquad (1)$$

$$H_2O \xrightarrow[\text{OX}]{-e^-} \cdot OH + H^+ \qquad (2)$$

$$C_x + H_2O \xrightarrow[OX]{-e^-} C_xOH + H^+ \tag{3}$$

$$C_x + 2H_2O \xrightarrow[OX]{-4e^-} C_{x-1} + 4H^+ + CO_2\uparrow \tag{4}$$

$$C_x + 2H_2O \xrightarrow[OX]{-3e^-} C_{x-1}COOH + 3H^+ + CO_2\uparrow \tag{5}$$

The pivotal role played by radicals is fully supported by experiments carried out at lower potential, where water is not dissociated (-0.733 to $+1.067$ V) and therefore no radical species are formed (Figure S4 in the Supporting Information). Actually, under these conditions the GOQDs are not released in the electrolyte.

The huge amount of radicals within the electrical double layer can possibly break up the intramolecular bonds in the dopant molecules, with the formation of several types of functional groups, as evidenced by XPS measurements (see section 3.2). These molecular fragments can eventually be covalently bound to the WE (Figure 1, step 1), where they can also undergo further reactions.

As is well reported in the literature, during the electrochemical cycling (Figure 1, step 2) the formation of linear chains of epoxy groups and carbonyl pairs[51−53] determines the unzipping of GO through the breaking of C−C bonds, with the consequent release in solution of doped GOQDs decorated at the edges by oxygen groups (Figure 1, step 3).[36,53] Figure 1 reports a schematization of the overall process, together with a digital picture of final GOQD solutions obtained from the electrochemical etching of the GO WE, in the presence of the different dopant molecules.

3.2. Chemical and Structural Characterization. XPS measurements were performed to determine the chemical composition of the doped GOQDs. The XPS survey spectra reported in Figure S5 (Supporting Information) show a predominant graphite C 1s photoemission line at a binding energy (BE) of 284.6 eV and an O 1s photoemission peak centered at 531.6 eV. The C/O atomic ratios are almost equivalent, with slight differences, for all doped GOQDs, and they are equal to 4.3. The pure GOQDs show a slightly lower C/O atomic ratio, which is equal to 3.8. Figure S5 (Supporting Information) shows the presence of B and N 1s photoemission lines in the survey spectra of B- and N-doped GOQDs (hereafter B- and N-GOQDs), respectively. On the other hand, both B and N 1s peaks are visible in the survey spectrum of B,N-*co*-doped GOQDs (hereafter B,N-GOQDs). These findings confirm the successful introduction of heteroatoms into the GOQDs by electrochemical etching of the GO WE in the dopant-containing electrolyte. Table 2 reports the elemental compositions (atom %) for all of the prepared systems, which are similar in terms of dopant concentration to those already reported in the literature for analogous materials.[54a,b,55]

In order to have a better understanding of the different chemical species introduced by the doping, the photoemission

Table 2. Elemental Composition (Calculated from XPS Quantitative Analysis) for the Doped and Codoped Systems Studied in This Work

	B (atom %)	N (atom %)
B-GOQDs	5.3	
N-GOQDs		5.1
B,N-GOQDs	5.2	4.7

spectra of carbon and dopants were separated into single chemically shifted components, as reported in Figure 2.

The multipeak analysis of the C 1s photoemission line of pure GOQDs (Figure 2a) indicates the presence of a graphite sp^2 core (284.6 eV), whose edges are decorated by several oxygen functional groups, such as C−O (286.4 eV), C=O (288.1 eV), and O−C=O (289.2 eV).[53,56]

In the case of B-GOQDs, the B 1s fit reveals (see Figure 2b) the presence of three different B-based chemical defects. The first component (**1**), centered at 189.6 eV, is related to B substituting C in the sp^2 network.[19,49] This component has its direct counterpart in the C 1s fit reported in Figure 2a (the component associated with B−C(sp^2) bonds is localized at 283.5 eV).[19,26,49,77] The other two B 1s components are related to B−O bonds (Figure 2b: namely, G-BO (**2**; 190.6 eV) and G-BO$_2$ (**3**; 192.0 eV).[19,49,77,78] The presence of these oxidized groups is connected to the interaction between the dopant molecule (or, as discussed above, its unstable molecular fragments) and the oxygen functional groups that decorate the GO surface[30] or that are introduced by the oxidation of water during the anodic sweep up to +3.0 V.[36] The present method allows the introduction of a high percentage of substitutional B atoms in the graphite core of the GOQDs (whose component counts for 27% of the total B 1s photoemission area). With regard to the N-GOQDs, from a comparison between the C 1s spectrum of pure and N-doped GOQDs (Figure 2a), a component connected to C−N groups can be identified at 285.8 eV.[40,57] The multicomponent fit of the N 1s photoemission line, reported in Figure 2c, shows four different chemical components centered at BE values of 398.6, 399.9, 401.1, and 402.4 eV, which correspond to pyridine (**1**), pyrrole (**2**), graphite (**3**), and pyridine oxide groups (**4**), respectively.[58−61]

The main component of the N 1s photoemission line in the case of the synthesis with ethylenediamine (in parentheses data for 1,10-phenanthroline) is constituted by the pyrrolic N group (**2**), which counts for 41% (48%) of the total N 1s photoemission area; for both doping sources, pyridine (**1**) and graphite N (**3**) species are equivalently present in the N 1s spectrum, accounting for 25% (24%) and 27% (20%), respectively. Only 10% (5%) of the total N is present as an oxidized species, in which N is directly bonded to an O atom (**4**).

Interestingly, the use of a primary alkyl amine (ethylenediamine) or of an aromatic π-conjugated amine (1,10-phenanthroline) does not strongly influence the chemical state of nitrogen atoms transferred to the GOQDs.

This result is in agreement with the mechanism proposed for the preparation of doped GOQDs, which is mainly mediated by highly reactive radicals. This implies that the obtained doped GOQDs do not keep "chemical memory" of the particular structure of the parent dopant, and the number and the type of the functional groups introduced during the EC synthesis in the GOQDs depend only on the formation kinetics of the dopant radicals.

Since synergetic effects between different heteroatoms present in the graphite networks can promote an enhanced catalytic activity in several electrochemical reactions (and, in particular, in the ORR),[26,28,54,62] we employed a combination of ethylenediamine/phenyldiboronic acid in order to prepare B,N-GOQDs. The C 1s multicomponent fit (reported in Figure 2a) shows the presence of both C−N and B−C(sp^2) bonds (whose components are centered at 285.7 and 283.6 eV, respectively).
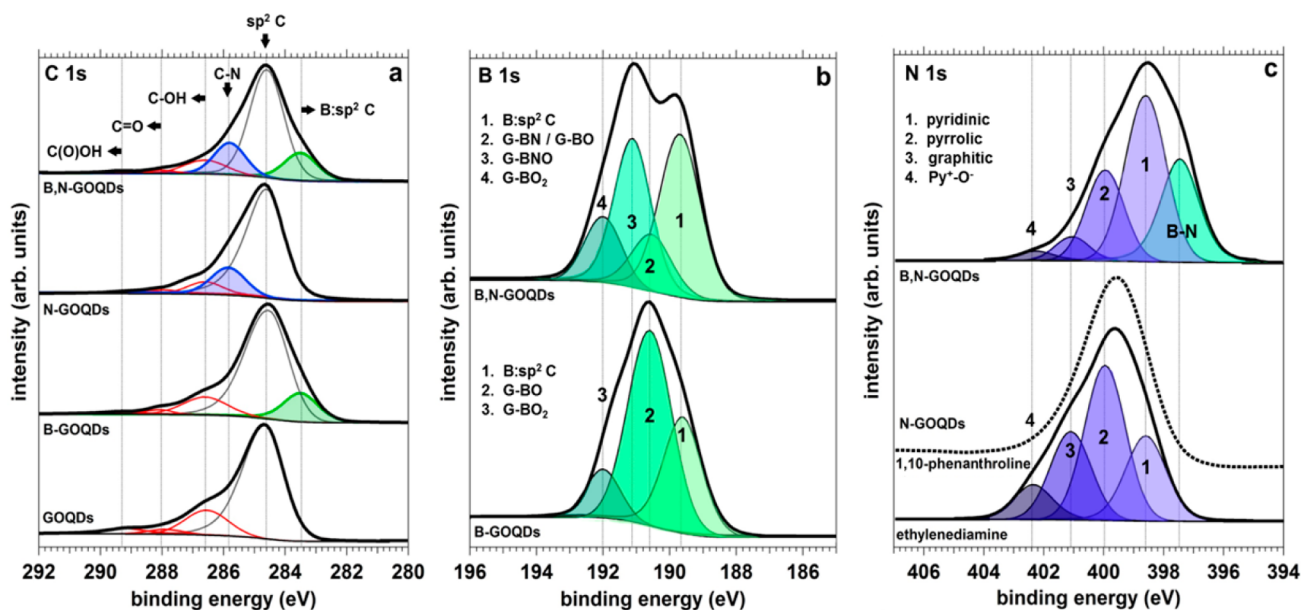
Figure 2. (a) Multicomponent fits of the C 1s XPS peaks for pure and B-, N-, and B,N-doped GOQDs. (b, c) Relative dopant photoemission line fits for B 1s and N 1s, respectively.

Figure 3. STM topographies (10 × 10 nm) of pure (a) and doped (b−d) GOQDs at the HOPG/air interface: (a) GOQDs (E = 0.08 V, I = 100 pA); (b) B-GOQDs (E = 0.15 V, I = 150 pA); (c) N-GOQDs (E = 0.15 V, I = 100 pA); (d) B,N-GOQDs (E = 0.10 V, I = 250 pA). The scale bar is 2 nm.

Similarly, the B 1s photoemission spectrum reported in Figure 2b shows the presence of the B−C(sp^2) bond component (**1**) centered at 189.6 eV.[19,26,49,77] The B,N codoping affects the relative amount of the B−C(sp^2) bond, which changes from 27% in the case of B-GOQDs to about 38% in the case of B,N-GOQDs. With regard to the second component, centered at 190.6 eV (**2**), the small difference in the electronegativity between N and O (0.4) does not allow discriminating between the G-BO and the G-BN groups. Then, this component has to be identified as the envelope of the two single G-BO and G-BN components. This observation will be further supported by the photoemission data in section 3.3.2. The new peak, centered at 191.1 eV (**3**), is assigned to G-BNO groups: that is, boron atoms bonded to both nitrogen and oxygen.[78] This observation is also highlighted by the difference spectra reported in Figure S6 (Supporting Information), for the B and N 1s photoemission peaks. This directly proves that the codoping is not the simple sum of the two heteroatoms but involves a direct interaction between the two distinct dopants.[54,62] Figure 2b and Figu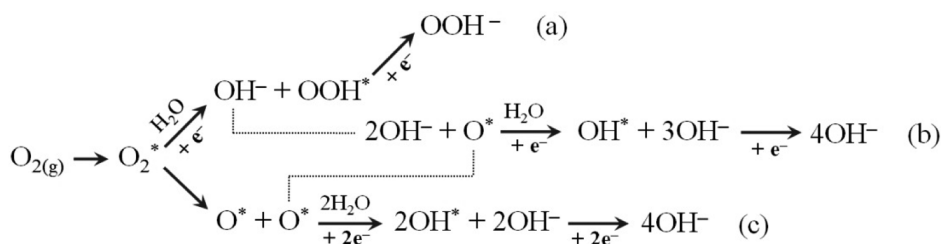re S6 show that the intensity of the B 1s photoemission peak in the case of the B,N-GOQDs is stronger at high BE with respect to the B-doped system. Similarly, an opposite phenomenon is observed in the N 1s photoemission peak, in which a clear shift toward low BEs takes place as a result of the

B−N bond formation. This can be explained by the large difference in the electronegativity of B and N (i.e., 1.0), which implies that the generation of direct B−N bonds causes an upshift of the B 1s peak (Figure S6a) and the concomitant downshift of the N 1s peak (Figure S6b), with respect to the signals of the singly doped systems.

The chemical state of N in B,N-GOQDs is elucidated by the identification of the chemically shifted components in the photoemission spectrum, as reported in Figure 2c. The formation of C−BN groups, observed in the B 1s data, is confirmed by the presence of a highly intense C−BN component in the N 1s spectrum, centered at 397.5 eV,[62,63] which represents 31% of the whole peak area. By making reference to the discussion reported above on N-GOQDs, we can also identify other four different chemically shifted components centered at 398.6, 400.0, 401.1, and 402.4 eV, which correspond to pyridine (**1**), pyrrole (**2**), graphite (**3**), and pyridine oxide groups (**4**), respectively. It is noteworthy that the B,N codoping seems to trigger a higher selectivity for the formation of pyridine groups (**1**) in the B,N-GOQDs, in comparison to the N-GOQDs. In fact, the pyridine component passes from 25% (in the case of N-GOQDs) to 39% (in the case of B,N-GOQDs). This could have important consequences in the catalytic properties of this material, since the carbon

$$O_{2(g)} \rightarrow O_2^* \xrightarrow[+\ \varepsilon]{H_2O} OH^- + OOH^* \xrightarrow{\times\ \varepsilon} OOH^- \quad (a)$$

$$2OH^- + O^* \xrightarrow[+\ e^-]{H_2O} OH^* + 3OH^- \xrightarrow{+\ e^-} 4OH^- \quad (b)$$

$$O^* + O^* \xrightarrow[+\ 2e^-]{2H_2O} 2OH^* + 2OH^- \xrightarrow{+\ 2e^-} 4OH^- \quad (c)$$

Figure 4. Possible ORR pathways in alkaline medium: (a) $2e^-$ pathway; (b,c) $4e^-$ reactions. Asterisks indicate the adsorbed species.
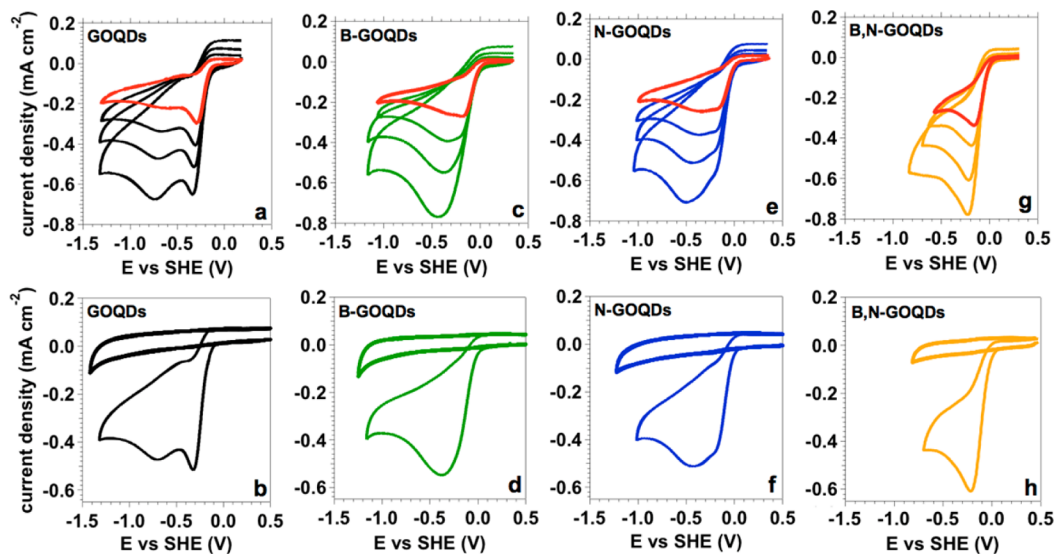
Figure 5. CVs of pure GOQDs (a) and B- (c), N- (e), and B,N-GOQDs (g) in O_2-saturated 0.1 M KOH solution, at different potential scan rates (10 (red curve), 20, 50, and 100 mV/s) and the corresponding CVs (b, d, f, h; scan rate 50 mV/s) acquired in Ar-saturated (thick curves) and O_2-saturated 0.1 M KOH solutions.

atoms close to pyridine groups are considered to be the active sites for the ORR,[64] especially under alkaline conditions.[54,65] At the same time, we observe a depletion of the content of pyrrole groups (**2**), (which passes from 41% in the case of N-GOQDs to 19% in the case of B,N-GOQDs) and in the content of N-graphite defects (**3**) (reduced from a value of 24% in the case of N-GOQDs to 9% in the case of B,N-GOQDs). Finally, the B,N codoping can efficiently reduce the amount of oxidized N groups (**4**), which decreases from 10% to 2% of the total peak area, with respect to the singly doped N-GOQDs.

STM measurements on diluted drop-casted solutions of GOQDs provide direct evidence of the presence of nano-fragmented GO. After the evaporation of the solvent, GOQDs can be adsorbed in a flatly lying geometry on a HOPG substrate, mainly due to $\pi-\pi$ interactions.[66] As experimentally observed, the surface diffusion of single GOQD units is relatively easy at room temperature, probably because the irregular structure of the GOQD edges weakens an effective interaction with the substrate. For this reason, mild tunneling conditions were used to limit unwanted tip-induced diffusion. Generally, no lateral order is detected and single randomly scattered GOQDs are found. High-resolution topographies (Figure 3) indicate that the pure GOQDs display a quasi-circular shape (Figure 3a), whereas the B- and N-GOQDs (Figure 3b,c) show straight edges resembling triangular shapes. Straight and round mixed edges instead are visible on B,N-GOQDs (Figure 3d). These features are attributed to the exposure of specific graphite crystal faces[67,68] as a consequence of the unzipping reactions that originated the nanofragments.

All of the observed pure, doped, and codoped GOQDs fall into a 1 nm sharp size dispersion centered at 2 nm, with heights in the 0.4−0.6 nm range, confirming that the prepared GOQDs have a thickness of a single layer.[69] The STM contrast is substantially unaffected by variations in sign or magnitude of the applied voltage, and no atomic resolution could be achieved on the GOQDs. This is due to the close proximity of the edges and to the presence of different types of defects, which scatter the electron wave functions.[67,70a,b] This phenomenon may be also the reason for the experimental observation of the invariance of the STM contrast with respect to the applied voltage. To our knowledge, so far there have been no reports of direct visualization of defects (or dopant) on GQDs or on GOQDs by either STM or TEM, because of the intrinsic high complexity and defectivity of these materials. This is at variance with the investigation on large (100 nm width) doped G sheets obtained by chemical vapor deposition, where advanced microscopic investigations provided a direct visualization of dopant atoms and defects.[71a,b,72,73]

3.3. Oxygen Reduction Reaction Catalytic Activity of Pure and Doped GOQDs. Apart from their unique photophysical properties (which will be addressed in another work), doped GOQDs are also expected to possess electro-catalytic activity toward the ORR, as widely reported in the literature. In particular, B-,[54,92] N-,[47,59,60,74,75,92] and S-doped[17,54,76,92] and B,N-codoped[14,25−27,77−79] G-based materials have shown high activities toward the reduction of oxygen, but these studies have been focused on 3D materials.[40,47,74,80] According to the best of our knowledge, only the work of Li et

Table 3. Potential Onsets (Derived by the Tangent Method), Peak Potentials, and Numbers of Electrons Exchanged during the Reduction of Oxygen (at Different Potential Values) for the As-Prepared Systems and after Chemical Reduction

	onset[a] (V)	$E_p{}^a$ (V)	n^a							
			E = −0.103	E = −0.203	E = −0.303	E = −0.403	E = −0.503	E = −0.703	E = −0.903	E = −1.103
GOQDs	−0.114	−0.300			2.21		2.23	2.24	2.23	2.22
B-GOQDs	0.003	−0.259			2.31		2.35	2.28	2.26	2.30
N-GOQDs	0.000	−0.246			2.28		2.27	2.24	2.23	
B,N-GOQDs	0.035	−0.177			2.50		2.49	2.48	2.62	
red-B-GOQDs	0.025	−0.165	3.47	3.61	3.69	3.82				
red-N-GOQDs	0.015	−0.157	2.86		3.36	3.42	3.78			
red-B,N-GOQDs	0.058	−0.119			3.87		3.91	3.92	3.94	

[a]All of the potentials are vs SHE. The values are calculated for a potential scan rate of 10 mV/s.

al.[81] reports the study of the catalytic properties of genuine GQDs per se, considered as distinct molecular units. Therefore, a study of the catalytic performances of the pure and doped GOQDs is still missing in the literature.

The reduction of oxygen catalyzed by graphite and G-based materials in alkaline electrolytes follows the reaction mechanism proposed by Strelko et al.,[82,83,92] reported schematically in Figure 4.

As is well-known in the literature,[65,83,92] ORR can occur, in accord with the scheme reported in Figure 4, either by a two-electron reaction (2e⁻, Figure 4a), with the formation of an OOH⁻ intermediate, or by a more efficient direct four-electron mechanism (4e⁻, Figure 4b,c).

Since the rate-determining step is represented by the desorption rate of OOH* or OH* species (which characterizes the selectivity of the catalytic material toward the 2e⁻ or 4e⁻ pathway, respectively),[83] it is clear that the increase in the kinetics of this electronic transfer plays a fundamental role in the catalytic performances toward the ORR.

To investigate the catalytic properties of our doped GOQDs, 100 nm films were drop-casted from concentrated aqueous solutions onto clean glassy carbon (GC), using Nafion[84] as the binder polymer to enhance both the mechanical stability and proton and OH⁻ permeability of the material.[84] SEM micrographs of the prepared films are reported in Figure S7 (Supporting Information).

Following this procedure, it was possible to investigate the real electrochemical response of the doped GOQDs without performing any further preparation, different from what has been currently reported in the literature,[40,47] which may change the chemical nature or the molecular structure of the quantum dots themselves.

Figure 5 reports the polarization curves for the O₂ reduction on pure GOQDs (a) and B- (b), N- (c), and B,N-GOQDs (d), acquired in O₂-saturated KOH 0.1 M solution. Every system shows a well-defined cathodic feature for the irreversible reduction of O₂. As reported in Table 3, the doped systems display a positive shift of the onset potential with respect to pure GOQDs, indicating that the introduction of the heteroatoms promotes the catalytic activity for ORR as already reported in the literature.[40,47,54,58,60,74]

In the case of boron doping, the presence of substitutional atoms has a dual effect: on the one hand, since the electronegativity in boron is lower than that in carbon, the positively polarized boron atoms in the graphite lattice attract the nucleophilic oxygen molecules leading to efficient chemisorption; on the other hand, boron sites can also act as electron shuttles for the electron density of the graphite π-electron system going through the p_z orbital of boron to the chemisorbed O₂ molecule.[85,86] With regard to the N-GOQDs, although it is well-established that the introduction of N doping can boost the ORR catalytic activity of carbon-based materials,[40,47,59,61,74,75,81,87,92] the identity and the exact role of the electrocatalytically active centers are still a topic of debate. Recent works by Lai et al.[60] and Xing et al.[64] suggest that the carbon atom next to a pyridine nitrogen is involved in the reaction with oxygen, favoring its adsorption and further reaction. More generally, it is commonly accepted[60,88,89] that N-based defects in G increase the density of π states near the Fermi level with the consequent reduction of the work function. The relatively high electron-withdrawing power of N atoms reduces the electron density on the adjacent C nuclei, with a net charge transfer from C to N. Furthermore, N atoms can back-donate electrons to the adjacent C p_z orbitals involved in the π-conjugated system. The donation and back-donation processes facilitate the O₂ adsorption on the C atoms nearest to the N atom, and then the subsequent dissociation is in accord with the scheme reported in Figure 4. This determines a faster kinetics in the reduction of oxygen and then a lower overpotential needed for the reaction. To conclude, the loss of the electroneutrality of graphite materials to create charged sites favorable for O₂ adsorption seems to be a key factor for enhancing ORR activity,[90] regardless of whether the dopants are B or N atoms.[60,61,92]

Concerning the codoped GOQDs, they are characterized by the highest activity for the reduction of oxygen (i.e., lowest overpotential), in comparison to the performances shown by the other materials.[26,62]

The origin of this behavior is quite difficult to trace; however, the photoemission data clearly indicate that the presence of nitrogen determines a shift toward higher BE in the centroid of the photoemission peak of boron, which indicates an average higher positive charge on boron sites, which therefore can be more efficient in the adsorption of oxygen. Moreover, in B,N-GOQD materials there is an increase in the pyridine component, apparently stabilized by the presence of boron, supporting the idea that these sites are indeed the most active players involved in the ORR.

3.3.1. ORR Mechanism for Pure and Doped GOQDs. In order to obtain the number of the exchanged electrons and, in this way, to clarify the mechanism of the reduction of oxygen on the doped GOQDs, we carried out rotating disk electrode (RDE) measurements.

Linear sweep voltammetry (LSV) curves of the ORR on the studied systems are reported in Figure 6 for different electrode rotation speeds. The measured current densities show a typical
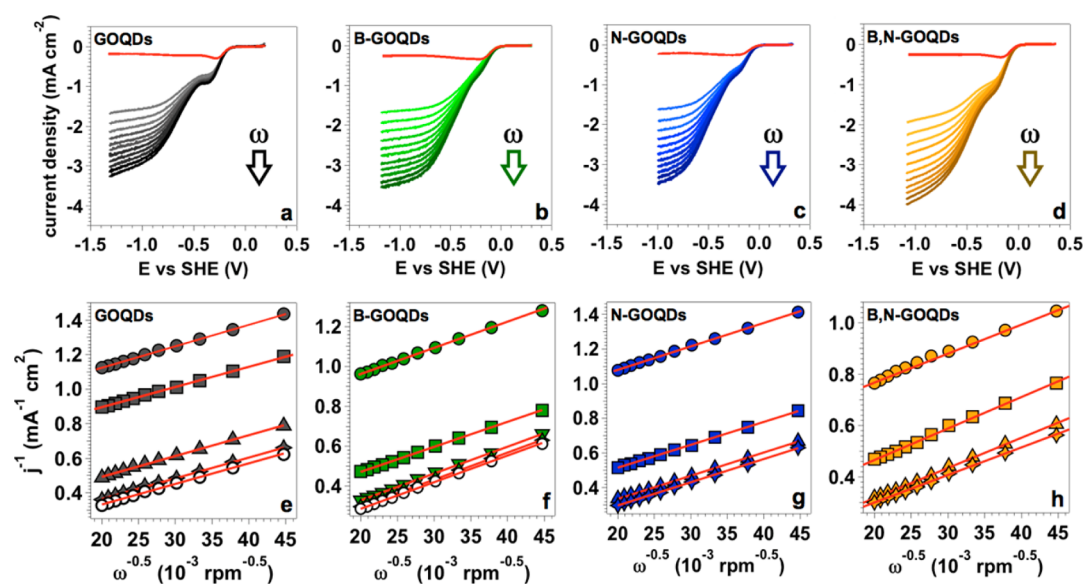
Figure 6. RDE linear sweeps for pure GOQDs (a) and B- (b), N- (c), and B,N-GOQDs (d) acquired in O_2-saturated 0.1 M KOH solution, for different WE rotation rates ranging from 500 to 2500 rpm (the red lines are the polarization curves acquired without rotation) and (e−h) corresponding Koutecky−Levich plots for pure GOQDs (e) and B- (f), N- (g), and B,N-GOQDs (h), for different potentials derived from the RDE measurements (dots, −0.303 V; squares, −0.503 V; triangles, −0.703 V; stars, −0.903 V; circles, −1.103 V).

increase as the electrode rotation rate increases, due to the enhanced diffusion of electrolytes.[91,92] The transferred electron number per O_2 molecule involved in the ORR process and, therefore, the predominant reaction pathway were determined using the Koutecky−Levich formalism (details are provided in the Supporting Information). The parallel and straight fitting lines, reported in Figure 6 for each system and for different potential values across the LSV, imply a first-order reaction with respect to dissolved oxygen.[92] Interestingly, the n values for pure GOQDs and B-, N-, and B,N-GOQDs are close to 2, as reported in Table 3, with just minor changes as a function of the potential. Apparently, the production of peroxide-based intermediates (as described by the 2e$^−$ mechanism reported in Figure 4) is in contradiction with the commonly accepted 4e$^−$ pathway for the reduction of oxygen on doped G and GO QDs.[15,47,54,60,61,74] However, in the cited literature papers, the G-based QDs were employed merely as a "dopant source" for 3D-structured materials.[40,47] On the other hand, the size of the sp^2 lattice influences the ORR behavior.[92] It has been reported in fact that the reduction in the lateral size of N-doped G QDs, up to the nanometer scale, leads to a significant enhancement in the hydrogen peroxide production, even in alkaline electrolytes.[81]

Moreover, not only the size but also the chemical composition of the as-prepared pure and doped GOQDs strongly influences the selectivity toward the reduction of oxygen. As has been well studied in the literature, the presence of oxygen functional groups decorating the graphite nano-platelets influences the catalytic activity and, in particular, the O_2 reduction pathway: oxygen moieties such as quinones, anthraquinones, and hydroquinones on graphite-based material (highly oriented pyrolytic graphite (HOPG) and glassy carbon (GC)) leads to a 2e$^−$ reaction pathway, with the consequent production of hydrogen peroxide.[93a−h] In contrast, chemically modified graphite materials with low concentrations of oxygen groups such as N-doped HOPG show a selective pathway reduction of oxygen to water.[87,94]

Thence, our results are in line with these previous data, showing that the introduction of dopant atoms (N or B) positively enhances the catalytic activity of the GOQDs. The high selectivity of the as-prepared pure or doped GOQDs toward the two-electron reaction path suggests their application as nanocatalysts for the selective production of H_2O_2 to be used in water remediation or organic microflow synthesis.

3.3.2. Role of the Oxygen Functional Groups in the ORR Mechanism. Chemical Reduction of Doped GOQDs. In order to point out the role played by the oxygen functional groups, decorating the edges of the doped GOQDs, on the activity and selectivity toward the ORR, we have performed a mild chemical reduction with NaBH$_4$ (for 12 h at room temperature; see the Supporting Information for details). Figure 7 reports the multipeak analysis of C 1s and of the dopant core level photoemission lines for B- and N-GOQDs after the chemical reduction (hereafter red-B-GOQDs and red-N-GOQDs, respectively).

In both cases, the chemical reduction treatment determines an important decrease of the oxidized species, such as G-BO$_2$ and N−O groups present in the B- and N-GOQDs, respectively. Thus, after the chemical reduction the doped GOQDs are characterized by a C sp^2 core with the presence of several dopant species (as discussed above), but with a very limited oxygen content: the C/O ratio passes from 4.3 for the as-prepared systems to about 10.6 in the case of the chemically reduced B-, N-, and B,N-GOQDs.

As shown in Figure 8, the removal of the oxygen functional groups on both systems goes together with an increase in the activity with respect to the as-prepared systems. In particular, in the case of B-GOQDs, the onset potential increases by 22 mV after the chemical reduction. Similarly, the peak potential undergoes a shift toward less cathodic potential, with a net overpotential gain of 94 mV after the NaBH$_4$ treatment (see Table 3).

The beneficial effect of the chemical reduction on the reactivity is also observed in the case of N doping. Figure 8 shows an oxygen reduction peak centered at −0.157 V in the
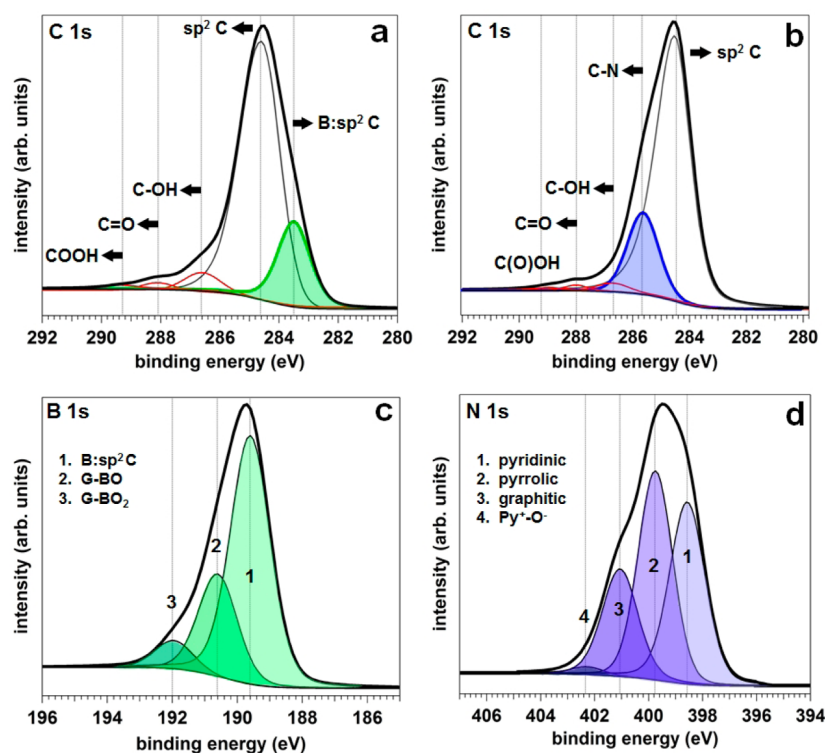
Figure 7. XPS analysis and relative fits of the C 1s (a, b) and B and N 1s (c, d) photoemission peaks for the red-B- and red-N-GOQDs, respectively.
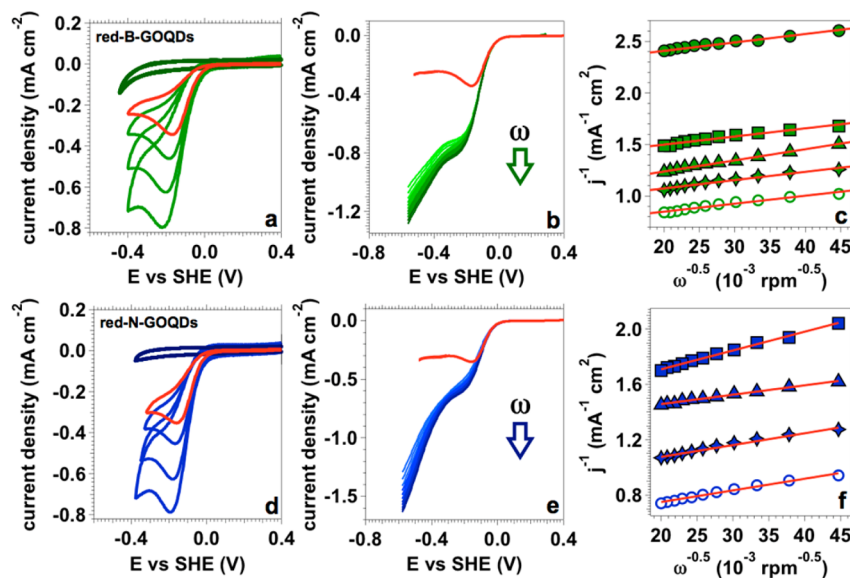
Figure 8. Catalytic tests for red-B- (a−c) and red-N-GOQDs (d−f); (a, d) CVs in O_2-saturated 0.1 M KOH solution, at different potential scan rates (10 (red curves), 20, 50, and 100 mV/s) and background polarization curves recorded in Ar-saturated 0.1 M KOH (at 50 mV/s, thick dark curves); (b, e) RDE linear sweeps acquired in O_2-saturated 0.1 M KOH solution, at a WE rotation rate ranging between 500 and 2500 rpm (the red lines are the polarization curves acquired without rotation); (c, f) Koutecky−Levich plots for different potentials derived from the RDE measurements (dots, −0.103 V; squares, −0.203 V; triangles, −0.303 V; stars, −0.403 V; circles, −0.503 V).

case of red-N-GOQDs, which is shifted upward by 89 mV with respect to the value observed on pristine N-GOQDs. Then, we can conclude that the removal of oxygen functional groups from the doped GOQDs represents a facile way to boost the catalytic activity of these systems: both B- and N-GOQDs exhibit an overpotential decrease of about 90 mV after the chemical reduction with NaBH$_4$.

Interestingly, the presence of oxygen groups influences not only the activity but also the selectivity of these materials

toward the two different paths followed by the ORR. Parts c and f of Figure 8 show that the number of exchanged electrons after the chemical reduction of B- and N-GOQDs is close to 4 for both systems. Since *n* was close to 2 for the as-prepared doped GOQDs, this confirms that the type of mechanism and therefore the selectivity of the ORR is driven by the presence[93f,g] or absence of the oxygen functional groups that decorate the doped GOQDs.
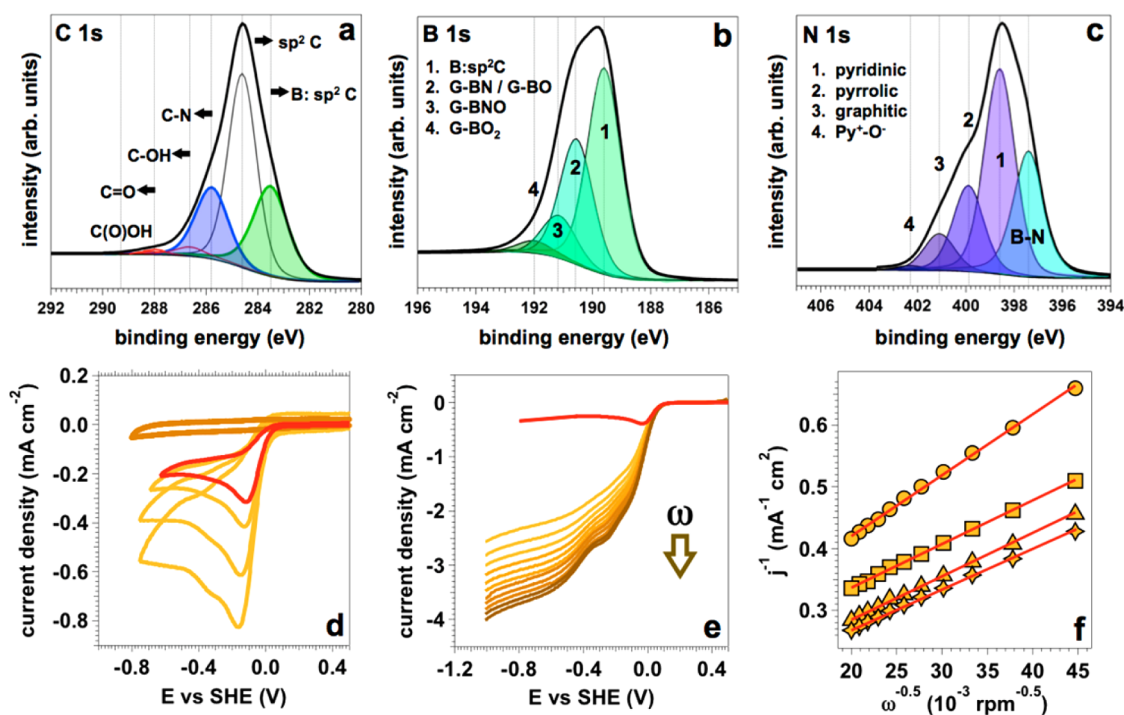
Figure 9. XPS analysis and catalytic tests for red-B,N-GOQDs: (a−c) multicomponent fits on B, C, and N 1s photoemission lines; (d) CVs in O_2-saturated 0.1 M KOH solution at different scan rates (10, (red curve) 20, 50, and 100 mV/s) and acquired in Ar-saturated 0.1 M KOH solution at 50 mV/s (background measurement, thick dark yellow curve); (e) RDE linear sweeps acquired in O_2-saturated 0.1 M KOH solution, at a WE rotation rate ranging between 500 and 2500 rpm (the red line is the polarization curve acquired without rotation); (f) Koutecky−Levich plots for different potentials derived from the RDE measurements (dots, −0.303 V; squares, −0.503 V; triangles, −0.703 V; stars, −0.903 V).
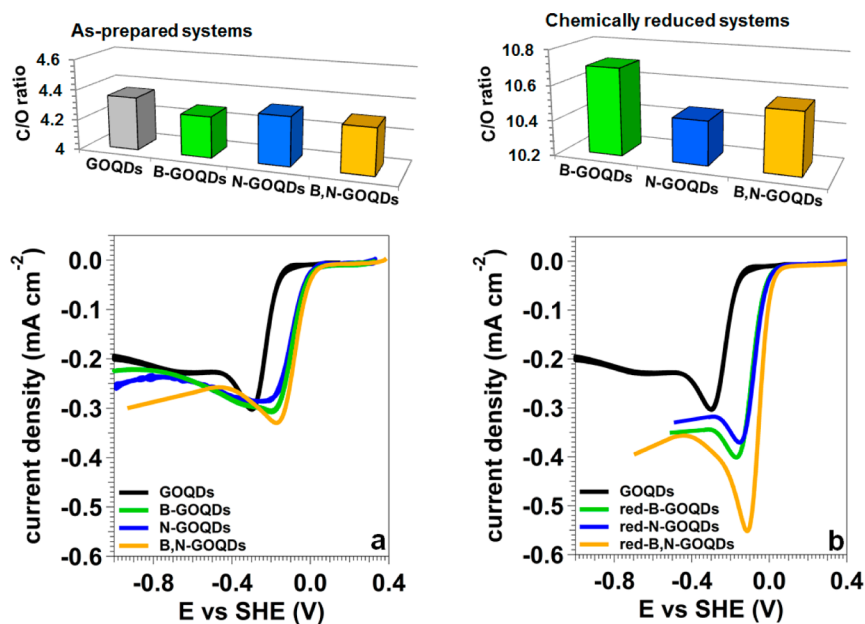
Figure 10. Polarization curves for the as-prepared (a) and for the chemically reduced systems (b), obtained in O_2-saturated KOH 0.1 M solution, at a scan rate of 10 mV/s. The headers report the C/O ratios for the different systems, before and after the chemical reduction.

This will be further discussed in the next section, where a theoretical modeling by DFT calculations is presented. In light of these findings, we have investigated the reduction effect with $NaBH_4$ on the doubly doped GOQDs, which are the most active and promising materials,[15,54,92] by a similar 4e$^-$ mechanism by eliminating the oxygen species by reduction with $NaBH_4$. Parts a−c of Figure 9 report the C, B, and N 1s photoemission lines, separated into chemically shifted components, for the B,N-GOQDs after the reduction procedure (hereafter red-B,N-GOQDs). The reduction treatment leaves substantially unchanged the chemical nature of the B,N-GOQDs, with the only exception of the oxidized components, which show a drastic decrease as a consequence of the reduction treatment.

Interestingly, the component labeled as **2** in Figure 9b exhibits an important intensity increase after the chemical

reduction treatment, whereas the oxidized G-BNO component (**3**) decreases. This can be explained by assuming that the G-BN groups are generated by the reduction of their relative oxidized precursor (that is, the G-BNO species) and noting that the B 1s BE is centered at 190.6 eV (overlapping in this way with the G-BO component, as already mentioned above in section 3.2). It is very important to note that the fully oxidized G-BO$_2$ component (**4**) practically disappears after the NaBH$_4$ treatment. The relative overall decrease of the oxidized species clearly improves the catalytic activity of the material. This will be further discussed in the next section of the theoretical modeling.

As shown in Figure 9d, the onset of the oxygen reduction peak is at −0.058 V, with a positive shift of 23 mV (with respect to the onset that characterizes the O$_2$ reduction peak of the B,N-GOQDs). The Koutecky−Levich linear fittings (Figure 9f) obtained from the RDE measurements at different rotation rates (Figure 9e) provide an average n value, over the potential range from −0.303 V to −0.903 V (see Table 3), of 3.71. This is in line with the results discussed above regarding the single B- and N-doping.

Figure 10 reports the polarization curves obtained for the different studied systems under quasi-steady-state conditions (scan rate 10 mV/s). For both the as-prepared and chemically reduced systems, the catalytic activity (as determined by the onset potential) follows the trend GOQDs < N-GOQDs ≅ B-GOQDs < B,N-GOQDs, highlighting the synergic effect of the concomitant boron and nitrogen doping of the graphite lattice.[27,62] Moreover, Figure 10 shows that the increase in the catalytic activity triggered by the chemical reduction process is accompanied by a general increase in the current densities. The slightly higher activity of B-doped materials with respect to those characterized by N-doping is in line with some other recent comparative works[83,95] and with some recent theoretical investigations.[96] We mention, however, that the peak potential of N-doped materials is better (i.e., lower in absolute value) with respect to B-doped systems. Actually some papers reports that N-doped G performs better than B-doped G.[16,97] These conflicting results can probably be connected to the different preparation methods used in the different works, which lead to materials with different chemical identities and therefore varied reactivities.

3.4. Theoretical Modeling. We have designed a number of *local* models for the ORR active sites for both oxidized and reduced doped and codoped GQDs, on the basis of the characterization data presented in section 3.2. They are based on a circumcoronene molecule where oxygen, boron, and nitrogen atoms are introduced to mimic locally the active sites. The size and the dopant concentration are close to the experimental values: 1.2 nm vs 1.5 nm and 2 atom % vs 4−5 atom %, respectively. The most relevant models, which will be discussed in the following, are presented by their atomic spheres representations in Figure 11. We consider the following three categories of doped species.

(a) *Oxidized*: for the B-doped systems, we propose a model with a dioxygenated boron (−BO$_2$) at the edge of the circumcoronene (B$_{edge}$O$_2$G), whereas for the B,N-codoped systems, we propose an analogous model with a next-neighbor edge pyridine N (B$_{edge}$O$_2$GN$_{edge}$).

(b) *Partially reduced*: for the B-doped systems, we propose a model with an oxygenated boron (−BO) at the edge of the circumcoronene (B$_{edge}$OG), whereas for the B,N-codoped
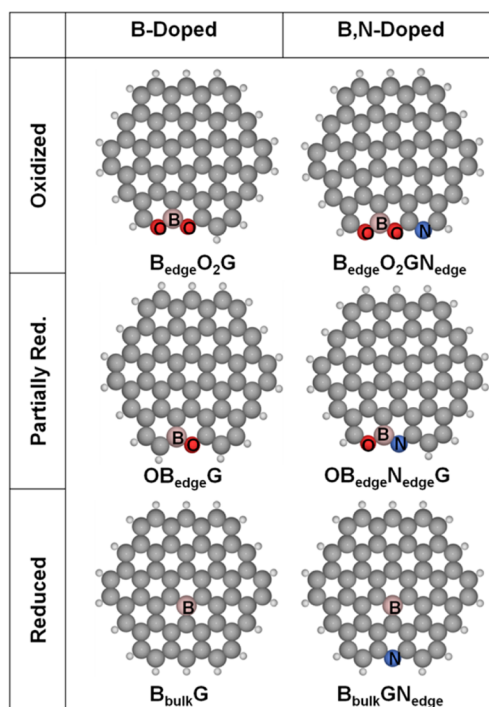
Figure 11. Atomic spheres representation of oxidized, and partially and fully reduced B- and B,N-GOQD models considered in this work.

systems, we propose a singly oxygenated species with bonded B−N atoms (OB$_{edge}$N$_{edge}$G).

(c) *Fully reduced*: for the B-doped systems, we propose a model with a three-coordinated boron (B−C(sp^2)) in the central hexagon of the circumcoronene (B$_{bulk}$G), whereas for the B,N-codoped systems, we propose an analogous model with an additional pyridine N at the edge of the circumcoronene model[27] (B$_{bulk}$GN$_{edge}$).

The fully reduced B-doped system (B$_{bulk}$G) has been the object of a previous very detailed study, which we refer to for further details in the methodology and approach.[98]

As a next step, for each of these model species of GQDs, we have determined the reaction intermediates and products of the ORR in alkaline solution, according to the associative reaction path (asterisks denote active surface sites) for the full 4e$^-$ process (see also Figure 4):

$$O_2(g) + * \rightarrow {}^*O_2 \tag{6}$$

$$^*O_2 + H_2O + e^- \rightarrow {}^*OOH + OH^- \tag{7}$$

$$^*OOH + OH^- + e^- \rightarrow {}^*O + 2OH^- \tag{8}$$

$$^*O + H_2O + 2OH^- + e^- \rightarrow {}^*OH + 3OH^- \tag{9}$$

$$^*OH + 3OH^- + e^- \rightarrow * + 4OH^- \tag{10}$$
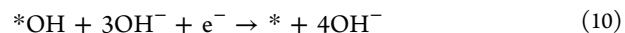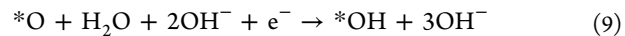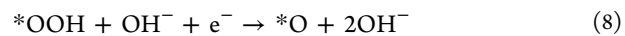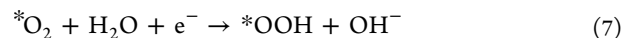
This was shown to be favored with respect to the dissociative path in our previous work,[95] as a consequence of the highly demanding steps for the O−O bond dissociation.

The first step of the reaction is the chemical adsorption of the O$_2$ molecule, which is not observed on undoped reduced QDs (pure circumcoronene). For all of the doped models presented above, the O$_2$ molecule preferentially adsorbs on the positively charged B atom (established by computing NBO charges).

In Figure 12 we show all the intermediates for the B,N-codoped circumcoronene models in terms of their atomic-
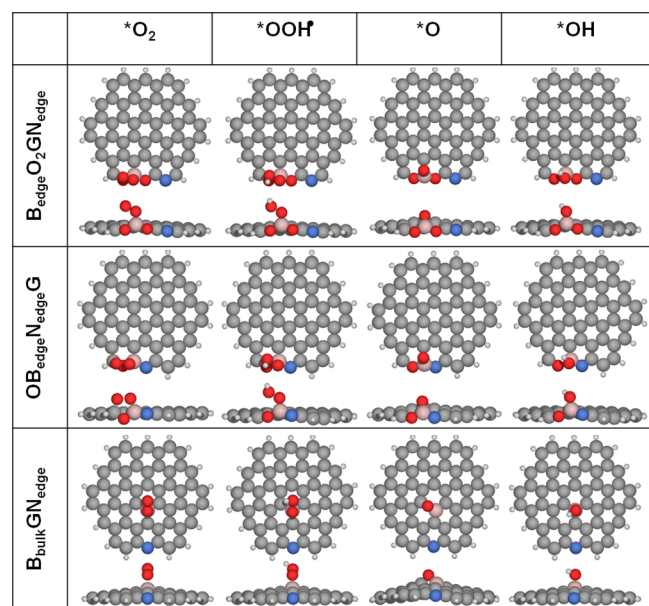
Figure 12. Atomic spheres representation of the ORR intermediates (top and side views) for the oxidized and partially and fully reduced B,N-GQD models along the associative reaction path. Asterisks denote the surface active sites. For the color assignment of the spheres to atomic species refer to Figure 11.

spheres representation. The corresponding structures for the B-GQDs are not shown, since they are essentially analogous. These representations clearly highlight that the chemisorption of oxygen-containing species (O_2, OOH, O, OH) causes some structural distortion of the systems with the B atom coming out of the graphite plane. The most distorted species is *O on the red-B,N-GOQDs ($B_{bulk}GN_{edge}$). It is interesting to note that the $-BO_2$ and $-OBN$ fragments ($B_{edge}O_2GN_{edge}$ and $OB_{edge}N_{edge}G$) are quite capable of binding a third or second O atom, since the B atom is a highly positive and, thus, acidic site. It is evident that the chemical natures of the intermediates (*O_2, *OOH, *O, and *OH) for the oxidized and reduced QDs are very different. This is expected to have a strong effect on their relative stability with respect to reactants and products of the ORR.

In order to analyze this aspect in further detail, we have resorted to the methodology developed by Nørskov and co-workers[44] for the ORR electrocatalysis by metal surfaces. This approach is based on the construction of free energy diagrams of reactants, intermediates, and products along the ORR reaction path, setting the free energy reference level at the value of the reaction products (* + 4OH⁻, for the 4e⁻ path under alkaline conditions). Additionally, within this methodology it is possible to consider the effect of an applied external bias U by shifting the free energy of each reduction step by $-eU$, where U is the electrode potential and e is the elementary charge. The value of $U = -0.303$ V (vs SHE) was chosen to resemble one of the investigated experimental potentials, as reported in Table 3, so that a direct link between the theoretical outcomes and the experimental observations exists. By applying this bias and the correction for a pH value of 13 (see the computational details in section 2), we obtain the diagrams in Figure 13. We first focus our attention on the 4e⁻ path, diagrams for which are

reported on the left side of each panel (black line). At first glance it is evident that the reaction energy profile for the oxidized species, of both B (a) and B,N-GOQDs (b), is very different from the corresponding red-B- and red-BN-GOQDs (left side of panels (c)−(f)). Note that the degree of reduction has a very small influence on the profile of the 4e⁻ path; thus, the left panels of (c) and (d) are very similar to the corresponding left panels of (e) and (f). For all reduced species we observe a downhill profile along the four reduction steps with a very large free energy gain (highlighted by blue arrows) associated with the second step, which reduces *OOH to *O, through the release of OH⁻ in solution. Differently, for the oxidized species of both B- and B,N-GOQD models, the free energy profiles of the 4e⁻ path are not a cascade, since the last reduction step, involving the release of the last OH⁻, is an uphill process (see blue arrows in left panels (a) and (b)). This is the major and critical difference between oxidized and reduced models.

Then, we analyze the 2e⁻ path, which consists of the following steps (see also Figure 4):

$$O_2(g) + * \rightarrow {}^*O_2 \tag{11}$$

$${}^*O_2 + H_2O + e^- \rightarrow {}^*OOH + OH^- + OH^- \tag{12}$$

$${}^*OOH + OH^- + e^- \rightarrow * + OOH^- + OH^- \tag{13}$$
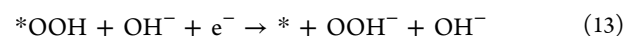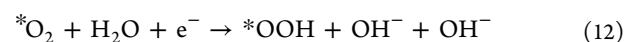
The oxygen adsorption (eq 11) and the first reduction step (eq 12), forming *OOH, are the same as for the 4e⁻ path (eqs 6 and 7). On the other hand, the second reduction step (eq 13) along the 2e⁻ path leads to the release of a hydroperoxide species (OOH⁻) in solution and can be competitive with eq 8 of the 4e⁻ path, where the O−O bond in *OOH is broken, releasing OH⁻ in solution and leaving *O on the surface.

The free energy diagrams of the 2e⁻ paths are reported on the right side of each panel in Figure 13 (red line). In the case of the fully reduced species (panels (e) and (f)), the two reduction steps are characterized by a downhill profile. However, the energy gain for the second reduction step, releasing OOH⁻ species in solution, is definitely much smaller than the second reduction step for the corresponding 4e⁻ path. For this reason we can safely conclude that, in the case of fully reduced species, the 4e⁻ path is favored with respect to the 2e⁻ path, in line with the experimental findings reported in the previous paragraph. Differently, in the case of oxidized species (panels (a) and (b)), the last reduction steps for both the 2e⁻ and 4e⁻ pathways are uphill, by about the same amount of free energy; therefore, we expect that in this case the 2e⁻ path becomes competitive with the 4e⁻ path, again in line with what is observed experimentally and discussed in previous paragraphs.

The free energy diagrams of the 2e⁻ paths are reported on the right side of each panel (red line). In the case of the fully reduced species (Figure 13, panels (e) and (f)), the two reduction steps are characterized by a downhill profile. However, the energy gain for the second reduction step, releasing OOH⁻ species in solution, is definitely much smaller than the second reduction step for the corresponding 4e⁻ path. For this reason we can safely conclude that, in the case of fully reduced species, the 4e⁻ path is favored with respect to the 2e⁻ path, in line with the experimental findings reported in the previous paragraph. The partially reduced species (panels (c) and (d)) in most respects are analogous to the fully reduced species, with the exception of a small barrier for the first
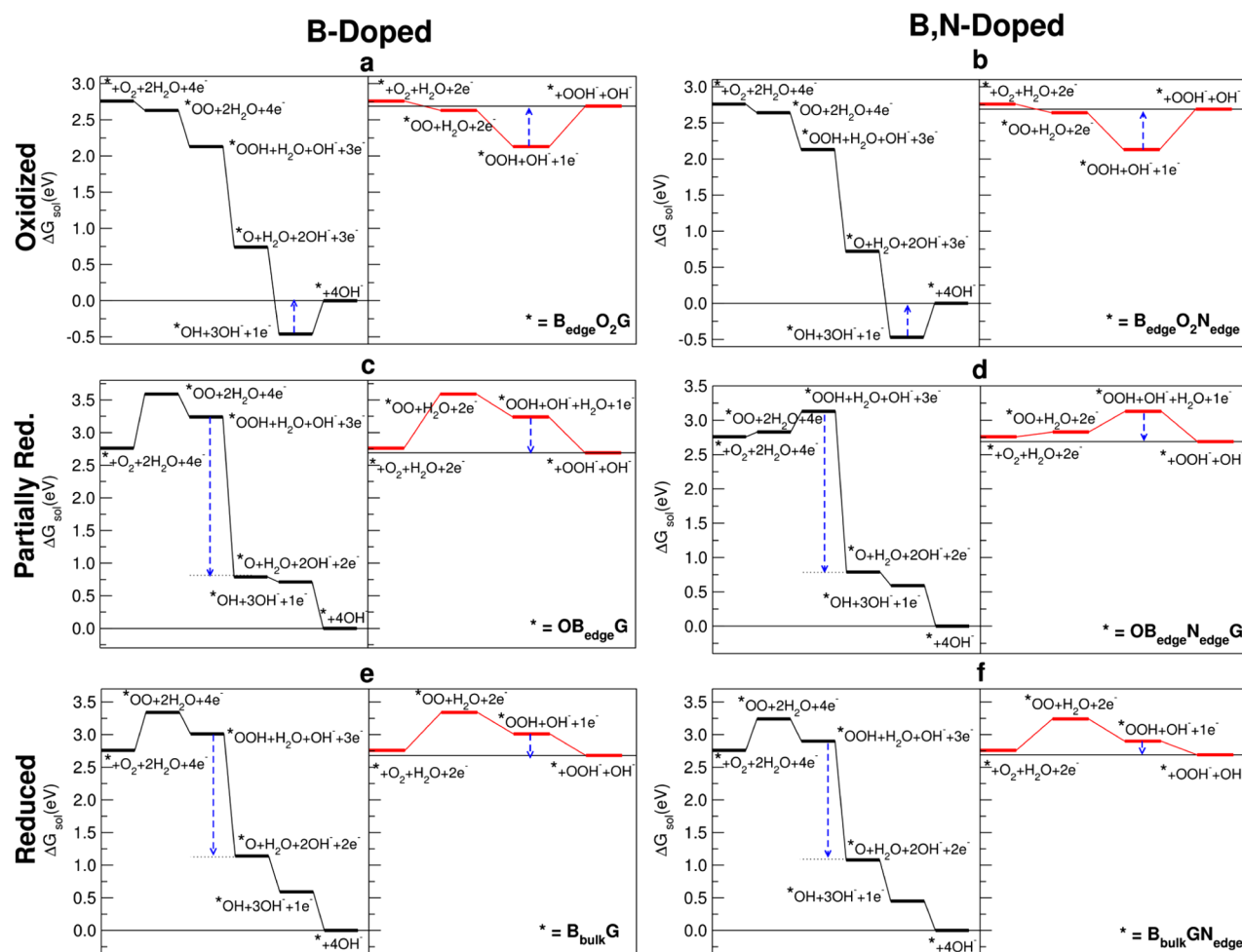
Figure 13. Free energy reaction profiles for the 4e⁻ (black line) and 2e⁻ (red line) pathways of the ORR reaction in aqueous solution (pH 13) at the external applied potential $U = -0.303$ V vs SHE, as catalyzed by B- or B,N-GOQD models in Figure 10. Blue dotted arrows indicate the most relevant reaction steps determining the 4e⁻/2e⁻ selectivity, as discussed in the text.

reduction step by the B,N-codoped species, as a consequence of a relative stabilization of the *OO intermediate, which, however, does not alter the 4e⁻/2e⁻ selectivity. Differently, in the case of oxidized species (panels (a) and (b)), the last reduction steps for both the 2e⁻ and 4e⁻ pathways are uphill, by about the same amount of free energy; therefore, we expect that in this case the 2e⁻ path becomes competitive with the 4e⁻ path, again in line with the experimental findings discussed in the previous paragraphs. Thus, we may conclude, from the analysis presented above, that the role of dopants in the GQDs is more effective under reducing conditions, since they push the selectivity toward the 4e⁻ path (full ORR) with downhill free energy profiles, at experimental external applied potentials (i.e., −0.303 V vs SHE).

4. CONCLUSION

We have reported a systematic study on the preparation and electrochemical characterization of singly and doubly doped GOQDs, together with the DFT investigation of a set of models consistent with the photoemission analysis.

From a methodological point of view, the use of GOQDs allowed us to investigate for the first time the most fundamental defects of G materials: functionalized edges.

We demonstrated that oxidized GOQDs are quite efficient for the selective production of H_2O_2 through a bielectronic

reduction of O_2. The introduction of dopants can boost the ORR: in particular, the B−N codoped materials show a very low overpotential. We rationalized the better performance of B,N-codoped GOQDs with respect to B- and N-doped GOQDs as due to (i) the twice higher concentration of active sites for ORR (B atoms and C atoms neighboring to N) and (ii) to an enhanced positive charge on B caused by the electron-withdrawing properties of N. In an upcoming paper we will demonstrate that the outstanding H_2O_2 selectivity of the oxidized doped GOQDs combined with their high activities can be efficiently exploited for water remediation applications. On the other hand, the chemical activity of doped GOQDs can be selectively tuned in order to follow a 4e⁻ reduction path (i.e., direct reduction of O_2 to water) simply by the chemical reduction with $NaBH_4$. This treatment has the effect of eliminating the oxygen species that are responsible for the competitive bielectronic reaction, as has also been observed in the literature.[93a−h]

Since we are dealing with GOQDs that are intrinsically semiconductive, the reduction process does not significantly affect the macroscopic electric properties as in micrometric GO sheets but has just a local effect on the functional groups. This is a strong indication that a highly conductive 3D structure is not necessary to achieve a high catalytic activity, whereas the pivotal point is to reduce the number of oxygenated species in

order to suppress the 2e⁻ reaction path to hydrogen peroxide.[93f,g] GOQDs therefore emerge as highly versatile nanocatalysts with an incredible potential for the realization of very efficient electroactive systems that, differently from 3D materials, could be used also for homogeneous catalysis. As a matter of fact, GQDs represent the extreme frontier of G nanotechnology, having a thickness of a single layer and being just a few nanometers wide, therefore exposing a huge fraction of highly active edges whose chemical nature can be easily modified to favor a specific functionality.

■ ASSOCIATED CONTENT

ⓈSupporting Information

The following file is available free of charge on the ACS Publications website at DOI: 10.1021/cs501211h.

> Experimental procedure for the preparation of GO via the modified Hummers method, spectroscopic (XPS, FT-IRAS, UV−vis, and Raman analyses) and morphological (SEM) characterization of the pristine GO, details of the electrochemical preparation of the pure and doped GOQDs, experimental details about the characterization techniques, proof of the synthesis radical-based mechanism of pure and doped GOQDs, XPS survey scans of pure and doped GOQDs, difference XPS spectra calculated between B and N 1s signals of B- and B,N-GOQDs, and SEM images of the pure and doped GOQD film used for the ORR electrochemical tests (PDF)

■ AUTHOR INFORMATION

Corresponding Authors

*E-mail fpr C.D.V.: cristiana.divalentin@unimib.it.
*E-mail for S.A.: stefano.agnoli@unipd.it

Notes

The authors declare no competing financial interest.

■ ACKNOWLEDGMENTS

■ REFERENCES

(1) Agnoli, S.; Granozzi, G. *Surf. Sci.* **2013**, *609*, 1−5.
(2) Zhu, Y.; Murali, S.; Cai, W.; Li, X.; Suk, J. W.; Potts, J. R.; Ruoff, R. S. *Adv. Mater.* **2010**, *22*, 3906−3924.
(3) Mkhoyan, K. A.; Contryman, A. W.; Silcox, J.; Stewart, D. A.; Eda, G.; Mattevi, C.; Miller, S.; Chhowalla, M. *Nano Lett.* **2009**, *9*, 1058−1063.
(4) Yamaguchi, H.; Eda, G.; Mattevi, C.; Kim, H.; Chhowalla, M. *ACS Nano* **2010**, *4*, 524−528.
(5) Wang, H.; Maiyalagan, T.; Wang, X. *ACS Catal.* **2012**, *2*, 781−794.
(6) Wang, X.; Li, X.; Zhang, L.; Yoon, Y.; Weber, P. K.; Wang, H.; Guo, J.; Dai, H. *Science* **2009**, *324*, 768−771.
(7) Shao, Y.; Zhang, S.; Engelhard, M. H.; Guosheng, L.; Guocheng, S.; Wang, Y.; Liu, J.; Aksay, I. A.; Lin, Y. *J. Mater. Chem.* **2010**, *20*, 7491−7496.
(8) Qu, L.; Liu, Y.; Baek, J.-B.; Dai, L. *ACS Nano* **2010**, *4*, 1321−1326.
(9) Jin, Z.; Yao, J.; Kittrell, C.; Tour, J. M. *ACS Nano* **2011**, *5*, 4112−4117.
(10) Usachov, D.; Vilkov, O.; Gruneis, A.; Haberer, D.; Fedorov, A.; Adamchuk, V. K.; Preobrajenski, A. B.; Dudin, P.; Barinov, A.; Oehzelt, M.; Laubschat, C.; Vyalikh, D. V. *Nano Lett.* **2011**, *11*, 5401−5407.
(11) Sun, Z.; Yan, Z.; Yao, J.; Beitler, E.; Zhu, Y.; Tour, J. M. *Nature* **2010**, *468*, 549−552.
(12) Deng, D.; Xiulian Pan, X.; Yu, L.; Cui, Y.; Jiang, Y.; Qi, J.; Li, W.-X.; Fu, Q.; Ma, X.; Xue, Q.; Sun, G.; Bao, X. *Chem. Mater.* **2011**, *23*, 1188−1193.
(13) Sheng, Z. H.; Shao, L.; Chen, J.-J.; Bao, W.-J.; Wang, F.-B.; Xia, X.-H. *ACS Nano* **2011**, *5*, 4350−4358.
(14) Choi, C. H.; Chung, M. W.; Kwon, H. C.; Park, S. H.; Woo, S. I. B. *J. Mater. Chem. A* **2013**, *1*, 3694−3699.
(15) Paraknowitsch, J. P.; Thomas, A. *Energy Environ. Sci.* **2013**, *6*, 2839−2855.
(16) Xue, Y.; Yu, D.; Dai, L.; Wang, R.; Li, D.; Roy, A.; Lu, F.; Chen, H.; Liu, Y.; Qu, J. *Phys. Chem. Chem. Phys.* **2013**, *15*, 12220−12226.
(17) Yang, Z.; Yao, Z.; Li, G.; Fang, G.; Nie, H.; Liu, Z.; Zhou, X.; Chen, X.; Huang, S. *ACS Nano* **2012**, *6*, 205−211.
(18) Poh, H. L.; Šimek, P.; Sofer, Z.; Pumera, M. *ACS Nano* **2013**, *7*, 5262−5272.
(19) Panchakarla, L. S.; Subrahmanyam, K. S.; Saha, S. K.; Govindaraj, A.; Krishnamurthy, R.; Waghmare, U. V.; Rao, C. N. R. *Adv. Mater.* **2009**, *21*, 4726−4730.
(20) Sheng, Z.-H.; Gao, H.-L.; Bao, W.-J.; Wang, F.-B.; Xia, X.-H. *J. Mater. Chem.* **2012**, *22*, 390−395.
(21) Lin, T.; Huang, F.; Liang, J.; Wang, Y. *Energy Environ. Sci.* **2011**, *4*, 862−865.
(22) Cattelan, M.; Agnoli, S.; Favaro, M.; Garoli, D.; Romanato, F.; Meneghetti, M.; Barinov, A.; Dudin, P.; Granozzi, G. *Chem. Mater.* **2013**, *25*, 1490−1495.
(23) Das, S.; Sudhagar, P.; Verma, V.; Song, D.; Ito, E.; Lee, S. Y.; Kang, Y. S.; Choi, W. B. *Adv. Funct. Mater.* **2011**, *21*, 3729−3736.
(24) Shen, B.; Jiangtao Chen, J.; Xingbin Yan, X.; Xue, Q. *RSC Adv.* **2012**, *2*, 6761−6764.
(25) Wang, S.; Zhang, L.; Xia, Z.; Roy, A.; Chang, D. W.; Baek, J.-B.; Dai, L. *Angew. Chem., Int. Ed.* **2012**, *51*, 4209−4212.
(26) Chang, C. H.; Chung, M. W.; Kwon, H. C.; Park, S. H.; Woo, S. I. *J. Mater. Chem. A* **2013**, *1*, 3694−3699.
(27) Zheng, Y.; Jiao, Y.; Ge, L.; Jaroniec, M.; Qiao, S. Z. *Angew. Chem., Int. Ed.* **2013**, *52*, 3110−3116.
(28) Liang, J.; Jiao, Y.; Jaroniec, M.; Qiao, S. Z. *Angew. Chem., Int. Ed.* **2012**, *51*, 11496−11500.
(29) Yang, S.; Zhi, L.; Tang, K.; Feng, X.; Maier, J.; Müllen, K. *Adv. Funct. Mater.* **2012**, *22*, 3634−3640.
(30) Dreyer, R.; Jia, H.-P.; Bielawski, C. W. *Angew. Chem., Int. Ed.* **2010**, *49*, 6813−6816.
(31) Pyun, J. *Angew. Chem., Int. Ed.* **2011**, *50*, 46−48.
(32) Baker, S. N.; Baker, G. A. *Angew. Chem., Int. Ed.* **2010**, *49*, 6726−6744.
(33) Kairdolf, B. A.; Smith, A. M.; Stokes, T. H.; Wang, M. D.; Young, A. N.; Nie, S. *Annual Rev. Anal. Chem.* **2013**, *6*, 143−162.
(34) Guo, C. X.; Dong, Y.; Yang, H. B.; Li, C. M. *Adv. Energy Mater.* **2013**, *3*, 997−1003.
(35) Lewotsky, K. *SPIE Newsroom* **2014**.
(36) Favaro, M.; Agnoli, S.; Cattelan, M.; Moretto, A.; Durante, C.; Leonardi, S.; Kunze-Liebhäuser, J.; Schneider, O.; Gennaro, A.; Granozzi, G. *Carbon* **2014**, *77*, 405−415.
(37) Hummers, W. S.; Offeman, R. E. *J. Am. Chem. Soc.* **1958**, *80*, 1339.
(38) Marcano, D.; Kosynkin, D. V.; Berlin, J. M.; Sinitskii, A.; Sun, Z.; Slasarev, A.; Alemany, L. B.; Lu, W.; Tour, J. M. *ACS Nano* **2010**, *4*, 4806−4814.

(39) Li, Y.; Hu, Y.; Zhao, Y.; Shi, G.; Deng, L.; Hou, Y.; Qu, L. *Adv. Mater.* **2011**, *23*, 776−780.

(40) Liu, Y.; Wu, P. *ACS Appl. Mater. Interfaces* **2013**, *5*, 3362−3369.

(41) Frisch, M. J.; Trucks, G. W.; Schlegel, H. B.; Scuseria, G. E.; Robb, M. A.; Cheeseman, J. R.; Scalmani, G.; Barone, V.; Mennucci, B.; Petersson, G. A.; Nakatsuji, H.; Caricato, M.; Li, X.; Hratchian, H. P.; Izmaylov, A. F.; Bloino, J.; Zheng, G.; Sonnenberg, J. L.; Hada, M.; Ehara, M.; Toyota, K.; Fukuda, R.; Hasegawa, J.; Ishida, M.; Nakajima, T.; Honda, Y.; Kitao, O.; Nakai, H.; Vreven, T.; Montgomery, J. A., Jr.; Peralta, J. E.; Ogliaro, F.; Bearpark, M.; Heyd, J. J.; Brothers, E.; Kudin, K. N.; Staroverov, V. N.; Kobayashi, R.; Normand, J.; Raghavachari, K.; Rendell, A.; Burant, J. C.; Iyengar, S. S.; Tomasi, J.; Cossi, M.; Rega, N.; Millam, M. J.; Klene, M.; Knox, J. E.; Cross, J. B.; Bakken, V.; Adamo, C.; Jaramillo, J.; Gomperts, R.; Stratmann, R. E.; Yazyev, O.; Austin, A. J.; Cammi, R.; Pomelli, C.; Ochterski, J. W.; Martin, R. L.; Morokuma, K.; Zakrzewski, V. G.; Voth, G. A.; Salvador, P.; Dannenberg, J. J.; Dapprich, S.; Daniels, A. D.; Farkas, Ö.; Foresman, J. B.; Ortiz, J. V.; Cioslowski, J.; Fox, D. J. *Gaussian 09, Revision D.01*; Gaussian, Inc., Wallingford, CT, 2009.

(42) Becke, A. D. *J. Chem. Phys.* **1993**, *98*, 5648−5652.

(43) Lee, C.; Yang, W.; Parr, R. G. *Phys. Rev. B* **1988**, *37*, 785−789.

(44) Nørskov, J. K.; Rossmeisl, J.; Logadottir, A.; Lindqvist, L.; Kitchin, J. R.; Bligaard, T.; Jonsson, H. *J. Phys. Chem. B* **2004**, *108*, 17886−17892.

(45) Tomasi, J.; Mennucci, B.; Cammi, R. *Chem. Rev.* **2005**, *105*, 2999−3093.

(46) Marenich, A. V.; Cramer, C. J.; Truhlar, D. G. *J. Phys. Chem. B* **2009**, *113*, 6378−6396.

(47) Li, Y.; Zhao, Y.; Cheng, H.; Hu, Y.; Shi, G.; Dai, L.; Qu, L. *J. Am. Chem. Soc.* **2012**, *134*, 15−18.

(48) Li, C.-J.; Chen, L. *Chem. Soc. Rev.* **2006**, *35*, 68−82.

(49) Fan, Z.; Li, Y.; Li, X.; Fan, L.; Zhou, S.; Fang, D.; Yang, S. *Carbon* **2014**, *70*, 149−156.

(50) Lu, J.; Yang, J.-X.; Wang, J.; Lim, A.; Wang, S.; Loh, K. P. *ACS Nano* **2009**, *3*, 2367−2375.

(51) Sun, T.; Fabris, S. *Nano Lett.* **2012**, *12*, 17−21.

(52) Li, Z.; Zhang, W.; Juo, Y.; Yang, J.; Hou, J. G. *J. Am. Chem. Soc.* **2009**, *131*, 6320−6321.

(53) Li, L.; Wu, G.; Yang, G.; Peng, J.; Zhao, J.; Zhu, J.-J. *Nanoscale* **2013**, *5*, 4015−4038.

(54) (a) Daems, N.; Sheng, X.; Vankelecom, I. F. J.; Pescarmona, P. P. *J. Mater. Chem. A* **2014**, *2*, 4085−4110. (b) Yang, Z.; Nie, H.; Chen, X.; Chen, X.; Huang, S. *J. Power Sources* **2013**, *236*, 238−249.

(55) Qu, D.; Zheng, M.; Du, P.; Zhou, Y.; Zhang, L.; Li, D.; Tan, H.; Zhao, Z.; Xie, Z.; Sun, Z. *Nanoscale* **2013**, *5*, 12272−12277.

(56) Favaro, M.; Agnoli, S.; Di Valentin, C.; Mattevi, C.; Cattelan, M.; Artiglia, L.; Magnano, E.; Bondino, F.; Nappini, S.; Granozzi, G. *Carbon* **2014**, *68*, 319−329.

(57) Dong, Y.; Pang, H.; Yang, H. B.; Guo, C.; Shao, J.; Chi, Y.; Li, C. M.; Yu, T. *Angew. Chem., Int. Ed.* **2013**, *52*, 7800−7804.

(58) Sheng, Z. H.; Shao, L.; Chen, J.-J.; Bao, W. J.; Wang, F. B.; Xia, X.-H. *ACS Nano* **2011**, *5*, 4350−4358.

(59) Sharifi, T.; Hu, G.; Jia, X.; Wågberg, T. *ACS Nano* **2012**, *6*, 8904−8912.

(60) Lai, L.; Potts, J. R.; Zhan, D.; Wang, L.; Poh, C. K.; Tang, C.; Gong, H.; Shen, Z.; Lin, J.; Ruoff, R. S. *Energy Environ. Sci.* **2012**, *5*, 7936−7942.

(61) Wu, G.; Zelenay, P. *Acc. Chem. Res.* **2013**, *46*, 1878−1889.

(62) Jin, J.; Pan, F.; Jiang, L.; Fu, X.; Liang, A.; Wei, Z.; Zhang, J.; Sun, G. *ACS Nano* **2014**, *8*, 3313−3321.

(63) Preobrajenski, A. B.; Vinogradov, A. S.; Mårtensson, N. *Surf. Sci.* **2005**, *582*, 21−30.

(64) Xing, T.; Zheng, Y.; Li, L. H.; Cowie, B. C. C.; Gunzelmann, D.; Qiao, S. Z.; Huang, S.; Chen, Y. *ACS Nano* **2014**, *8*, 6856−6862.

(65) Wong, W. Y.; Daud, W. R. W.; Mohamad, A. B.; Kadhum, A. A. H.; Loh, K. S.; Majlan, E. H. *Int. J. Hydrogen Energy* **2013**, *38*, 9370−9386.

(66) Hunt, A.; Dikin, D.; Kurmaev, E.; Lee, Y.; Luan, N.; Chang, G.; Moewes, A. *Carbon* **2014**, *66*, 539−546.

(67) Kobayashi, Y.; Fukui, K.; Enoki, T.; Kusakabe, K.; Kaburagi, Y. *Phys. Rev. B* **2005**, *71*, 193406/1−193406/4.

(68) Geim, A.; Novoselov, K. *Nat. Mater.* **2007**, *6*, 183−191.

(69) Pang, D.; Zhang, J.; Li, Z.; Wu, M. *Adv. Mater.* **2010**, *22*, 734−738.

(70) (a) Ritter, K.; Lyding, J. *Nat. Mater.* **2009**, *8*, 235−242. (b) Tapasztó, L.; Dobrik, G.; Lambin, P.; Biró, L. *Nat. Nanotechnol.* **2008**, *3*, 397−401.

(71) (a) Zhao, L.; He, R.; Taeg Rim, K.; Schiros, T.; Kim, K. S.; Zhou, H.; Gutiérrez, C.; Chockalingam, S. P.; Arguello, C. J.; Pàlovà, L.; Nordlund, D.; Hybertsen, M. S.; Reichman, D. R.; Heinz, T. F.; Kim, P.; Pinczuk, A.; Flynn, G. W.; Pasupathy, A. N. *Science* **2011**, *333*, 999−1003. (b) Zhao, L.; Levendorf, M.; Goncher, S.; Schiros, T.; Pàlovà, L.; Zabet-Khosousi, A.; Taeg Rim, K.; Gutiérrez, C.; Nordlund, D.; Jaye, C.; Hybertsen, M. S.; Reichman, D. R.; Flynn, G. W.; Park, J.; Pasupathy, A. N. *Nano Lett.* **2013**, *13*, 4659−4665.

(72) Lv, R.; Li, Q.; Botello-Méndez, A. R.; Hayashi, T.; Wang, B.; Berkdemir, A.; Hao, Q.; Elìas, A. L.; Cruz-Silva, R.; Gutiérrez, H. R.; Kim, Y. A.; Muramatsu, H.; Zhu, J.; Endo, M.; Terrones, H.; Chalier, J.-C.; Pan, M.; Terrones, M. *Sci. Rep.* **2012**, *2:586*, 1−8.

(73) Zhou, W.; Kapetanakis, M. D.; Prange, M. P.; Pantelides, S. T.; Pennycook, S. J.; Idrobo, J. C. *Phys. Rev. Lett.* **2012**, *109*, 206803.

(74) Zhang, Z.; Zhang, J.; Chen, N.; Qu, L. *Energy Environ. Sci.* **2012**, *5*, 8869−8890.

(75) Jeon, I.-Y.; Choi, H.-J.; Jung, S.-M.; Seo, J.-M.; Kim, M.-J.; Dai, L.; Baek, J.-B. *J. Am. Chem. Soc.* **2013**, *135*, 1386−1393.

(76) Jeon, I.-Y.; Zhang, S.; Zhang, L.; Choi, H.-J.; Seo, J.-M.; Xia, Z.; Dai, L.; Baek, J.-B. *Adv. Mater.* **2013**, *25*, 6138−6145.

(77) Choi, C. H.; Park, S. H.; Woo, S. I. *ACS Nano* **2012**, *6*, 7084−7091.

(78) Ozaki, J.-I.; Kimura, N.; Anahara, T.; Oya, A. *Carbon* **2007**, *45*, 1847−1853.

(79) Wu, Z.-S.; Winter, A.; Chen, L.; Sun, Y.; Turchanin, A.; Feng, X.; Müllen, K. *Adv. Mater.* **2012**, *24*, 5130−5135.

(80) Dai, L. *Acc. Chem. Res.* **2013**, *46*, 31−42.

(81) Li, Q.; Zhang, S.; Dai, L.; Li, L.-S. *J. Am. Chem. Soc.* **2012**, *134*, 18932−18935.

(82) Strelko, V. V.; Kartel, N. T.; Dukhno, I. N.; Kuts, V. S.; Clarkson, R. B.; Odintsov, B. M. *Surf. Sci.* **2004**, *548*, 281−290.

(83) Jiao, Y.; Zheng, Y.; Jaroniek, M.; Qiao, S. Z. *J. Am. Chem. Soc.* **2014**, *136*, 4394−4403.

(84) Mauritz, K. A.; Moore, R. B. *Chem. Rev.* **2004**, *104*, 4535−4585.

(85) Yang, L.; Jiang, S.; Zhao, Y.; Zhu, L.; Chen, S.; Wang, X.; Wu, Q.; Ma, J.; Ma, Y.; Hu, Z. *Angew. Chem., Int. Ed.* **2011**, *50*, 7132−7135.

(86) Ferrighi, L.; Datteo, M.; Di Valentin, C. *J. Phys. Chem. C* **2014**, *118*, 223−230.

(87) Favaro, M.; Perini, L.; Agnoli, S.; Durante, C.; Granozzi, G.; Gennaro, A. *Electrochim. Acta* **2013**, *88*, 477−487.

(88) Terrones, M.; Ajayan, P. M.; Banhart, F.; Blase, X.; Carroll, D. L.; Charlier, J. C. *Appl. Phys. A-Mater. Sci. Process.* **2002**, *74*, 355−361.

(89) Deng, D. H.; Pan, X. L.; Yu, L. A.; Cui, Y.; Jiang, Y. P.; Qi, J.; Li, W. X.; Fu, Q. A.; Ma, X. C.; Xue, Q. K.; Sun, G. Q.; Bao, X. H. *Chem. Mater.* **2011**, *23*, 1188−1193.

(90) Wang, S.; Yu, D.; Dai, L.; Chang, D. W.; Baek, J.-B. *ACS Nano* **2011**, *5*, 6202−6209.

(91) Levich, V. G. *Physicochemical hydrodynamics*, 2nd ed.; Prentice-Hall: Englewood Cliffs, NJ, 1962.

(92) Wang, D. W.; Su, D. *Energy Environ. Sci.* **2014**, *7*, 576−591.

(93) (a) Yaeger, E. *Electrochim. Acta* **1984**, *29*, 1527−1537. (b) Tammeveski, K.; Kontturi, K.; Nichols, R. J.; Potter, R. J.; Schiffrin, D. J. *J. Electroanal. Chem.* **2001**, *515*, 101−112. (c) Sarapuu, A.; Helstein, K.; Schiffrin, D. J.; Tammeveski, K. *Electrochem. Solid-State Lett.* **2005**, *8*, E30−E33. (d) Jürmann, G.; Schiffrin, D. J.; Tammeveski, K. *Electrochim. Acta* **2007**, *53*, 390−399. (e) McCreery, R. L. *Chem. Rev.* **2008**, *108*, 2646−2687. (f) Sarapuu, A.; Helstein, K.; Vaik, K.; Schiffrin, D. J.; Tammeveski, K. *Electrochim. Acta* **2010**, *55*, 6376−6382. (g) Kocak, I.; Ghanem, M. A.; Al-Mayouf, A.; Alhoshan, M.; Bartlett, P. N. *J. Electroanal. Chem.* **2013**, *706*, 25−32. (h) Mooste,

M.; Kibena, E.; Sarapuu, A.; Mäeorg, U.; Maia, G.; Tammeveski, K. *J. Solid State Electrochem.* **2014**, *18*, 1725−1733.

(94) Zhou, Y.; Holme, T.; Berry, J.; Ohno, T. R.; Ginley, D.; O'Hayre, R. *J. Phys. Chem. C* **2010**, *114*, 506−515.

(95) Zheng, Y.; Jiao, Y.; Ge, L.; Jaroniec, M.; Qiao, S. Z. *Angew. Chem., Int. Ed.* **2013**, *52*, 3110−3116.

(96) Sen, D.; Thapa, R.; Chattopadhyay, K. K. *ChemPhysChem* **2014**, *15*, 2542−2549.

(97) Xu, X.; Yuan, T.; Zhou, Y.; Li, Y.; Lu, J.; Tian, X.; Wang, D.; Wang, J. *Int. J. Hydrogen Energy* **2014**, *39*, 16043−16052.

(98) Fazio, G.; Ferrighi, L.; Di Valentin, C. *J. Catal.* **2014**, *318*, 203−210.